Near-Infrared-Absorbing Gold Nanopopcorns with Iron Oxide Cluster Core for Magnetically Amplified Photothermal and Photodynamic Cancer Therapy

Saheel Bhana,[†,∥] Gan Lin,[‡,∥] Lijia Wang,[§] Hunter Starring,[†,⊥] Sanjay R. Mishra,[§] Gang Liu,*[,‡] and Xiaohua Huang*[,†]

[†]Department of Chemistry, The University of Memphis, Memphis, Tennessee 38152, United States
[‡]State Key Laboratory of Molecular Vaccinology and Molecular Diagnostics & Center for Molecular Imaging and Translational Medicine, School of Public Health, Xiamen University, Xiamen, Fujian Province 361102, P. R. China
[§]Department of Physics, The University of Memphis, Memphis, Tennessee 38152, United States

Ⓢ Supporting Information

ABSTRACT: We present the synthesis and application of a new type of dual magnetic and plasmonic nanostructures for magnetic-field-guided drug delivery and combined photothermal and photodynamic cancer therapy. Near-infrared-absorbing gold nanopopcorns containing a self-assembled iron oxide cluster core were prepared via a seed-mediated growth method. The hybrid nanostructures are superparamagnetic and show great photothermal conversion efficiency (η = 61%) under near-infrared irradiation. Compact and stable nanocomplexes for photothermal−photodynamic therapy were formed by coating the nanoparticles with near-infrared-absorbing photosensitizer silicon 2,3-naphthalocyannie dihydroxide and stabilization with poly(ethylene glycol) linked with 11-mercaptoundecanoic acid. The nanocomplex showed enhanced release and cellular uptake of the photosensitizer with the use of a gradient magnetic field. In vitro studies using two different cell lines showed that the dual mode photothermal and photodynamic therapy with the assistance of magnetic-field-guided drug delivery dramatically improved the therapeutic efficacy of cancer cells as compared to the combination treatment without using a magnetic field and the two treatments alone. The "three-in-one" nanocomplex has the potential to carry therapeutic agents deep into a tumor through magnetic manipulation and to completely eradicate tumors by subsequent photothermal and photodynamic therapies without systemic toxicity.

KEYWORDS: iron oxide−gold nanopopcorns, hybrid nanoparticles, magnetic attraction, drug delivery, cancer, photothermal therapy, photodynamic therapy
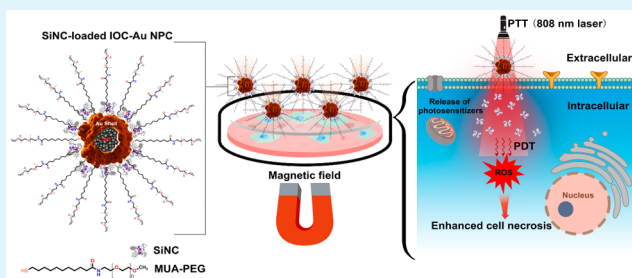
1. INTRODUCTION

One of the major current interests in nanomedicine is the use of near-infrared (NIR)-absorbing gold (Au) nanoparticles (NPs) for photothermal cancer therapy.[1] The rationale is that Au NPs exhibit strong localized surface plasmon resonance (LSPR) absorption. By changing the particle's structure or shape, the LSPR wavelength can be tuned into the tissue-transparent NIR region. Under laser irradiation, the NPs convert absorbed light quickly (on a picosecond time scale) into heat[2] that can ablate adjacent cancer cells. Since the therapeutic mechanism relies on a photophysical process, drug resistance and systemic toxicity associated with chemotherapy are avoided. During the past decade, different types of NIR-absorbing Au NPs have been reported and used for cancer photothermal therapy (PTT), including Au nanoshells,[3−5] nanorods (NRs),[6−9] nanocages,[10,11] hollow nanospheres,[12,13] and recently emerged nanopopcorns[14] and bellflowers.[15] Compared to traditional molecular photothermal agents,

these NPs have orders of magnitude higher light absorption efficiency.[16] They do not photobleach and allow for facile surface modification. When coated with polyethylene glycol (PEG), they show prolonged half-life in blood circulation,[17,18] which helps tumor uptake of the NPs and their cargos through the enhanced permeability and retention (EPR) effect.

Another light-mediated treatment that uses a chemical mechanism to kill cancer cells is photodynamic therapy (PDT). In PDT, a photosensitizer (PS) absorbs light energy and is excited from the ground state to a high energy state, which transfers energy to neighboring oxygen, leading to production of high energy reactive oxygen species (ROS) (mainly singlet oxygen) to kill cancer cells.[19−21] The major problem for traditional PDT was the target specificity of the PS

agents. Substantial efforts have been made to search for nanocarriers to improve PS delivery.[22−25] The use of photothermal NPs as PS carriers is advantageous over other carriers because cancer cells can be destroyed simultaneously by photothermal and photodynamic therapy under a single laser excitation. Combined PTT and PDT have been shown more effective than PTT or PDT alone due to additive or synergistic effects.[26−36]

We report here the synthesis and use of a new type of nanoplatform for combined cancer PTT and PDT. The NPs, which are Au nanopopcorns (NPCs) containing a self-assembled iron oxide cluster (IOC) core, are superparamagnetic and exhibit strong NIR absorption. Using the IOC−Au NPCs, we demonstrated the first application of magnetic−optical hybrid nanosystems for magnetic-field-guided drug delivery and dual mode PTT and PDT. Compared to existing PTT and PDT nanosystems, this new system has the potential to deliver both PDT and PTT agents deep into a tumor. It is well-known that tumor penetration of therapeutic agents remains a major issue in drug delivery and cancer treatment. Previously, Kong et al. reported that magnetic attraction, induced by gradient magnetic field from a permanent magnet, enhanced the accumulation of magnetic nanocapsules deep in a tumor by 200 fold as compared to that for the control group.[37] This opened new opportunities to deliver therapeutic agents deep into a tumor through magnetic manipulation. In this work, we effectively integrated the modalities of magnetic field-assisted drug delivery, PTT and PDT into a single nano-construct. We demonstrated through *in vitro* studies that combinatorial PTT and PDT with (w/) magnetic attraction is more effective than PTT and PDT without (w/o) magnetic attraction, PTT or PDT alone. The PS-loaded IOC−Au hybrid nanoplatform has great potential for highly effective tumor ablation and may prevent tumor recurrence. The hybrid NPs can also be used as a contrast agent for magnetic resonance imaging (MRI) and thus potentially offer a theranostic platform for tumor detection and therapy.

2. EXPERIMENTAL SECTION

Materials. All chemicals were purchased from Sigma-Aldrich unless specified. Amine-terminated poly(ethylene glycol) (PEG-NH$_2$, MW 5000) was purchased from Laysan Bio (Arab, AL).

Synthesis and Characterization of IO NPs and IOCs. IO NPs were synthesized by the thermal decomposition method developed by Sun et al.[38] Briefly, iron(III) acetylacetonate (2 mmol), 1,2-hexadecanediol (10 mmol), oleic acid (6 mmol), and oleylamine (6 mmol) were mixed in 1-octadecene (20 mL) in a three-neck bottle flask. The mixture was heated up to reflux (320 °C) under a nitrogen atmosphere for 1 h. After being cooled to room temperature, the resulting solution was added with ethanol to precipitate the particles. The NPs were concentrated by centrifugation, washed with hexane, and then resuspended in hexane for further use.

The IOCs were prepared according to our previously reported method[39] with modifications. In this method, 5 mg of IO NPs were dried under argon and mixed with 10 mg of N-alkyl polyethylenimine-(PEI) 2k in 500 μL of chloroform. The mixed solutions were added into 5 mL of distilled water under sonication. Then, the mixture was shaken for overnight and the chloroform was removed by rotary evaporation to obtain PEI-coated IOCs. The PEI-coated IOCs were dispersed in water for further use. The N-alkyl-PEI2k was prepared in advance by reacting 1-iodododecane with PEI2k in ethanol at 55 °C for 6 h, followed by solvent evaporation and purification with dialysis.

Synthesis and Characterization of IOC−Au NPCs. The PEI-coated IOCs were initially coated with a layer of negatively charged polymer to reverse the surface charge for subsequent growth of the Au

layer. This was done by mixing the clusters (0.2 mg/mL, Fe concentration in this paper) with polystyrene chloride (PSS, 20 mg/mL) in the presence of 20 mM sodium hydroxide for 30 min. After purification by magnetic separation, the PSS/PEI-coated IOCs were dispersed in water and used as seeds to make IOC−Au NPCs based on a seed-mediated growth method with modifications.[40] First, the PSS/PEI-coated IOCs (0.5 mL, 0.2 mg/mL) were adsorbed with diamminesilver ions (Ag(NH$_3$)$_2$$^+$) (20 μL, 10 mM), followed by reduction with sodium borohydride (NaBH$_4$) (100 μL, 10 mM) to form Ag-decorated IOCs. The Ag-decorated IOCs were purified by centrifugation and redispersed in ultrapure water to form the seed solution (0.5 mL, 0.2 mg/mL). In a separate glass flask, 45 mL of gold growth solution containing 0.1 M cetyl trimethylammonium bromide (CTAB), 0.4 mM chloroauric acid (HAuCl$_4$), and 80 μM AgNO$_3$ was prepared and heated to 25 °C in a water bath, followed by addition of 0.69 mL of 40 mM ascorbic acid (AA) to reduce HAuCl$_4$ to HAuCl$_2$. Then, 150 μL of the seed solution was injected and IOC−Au hybrid NPs formed within 2 h. The NPs were purified by 2 times of centrifugation and washing with ultrapure water. The absorption spectrum of the NPs was measured using an Ocean Optics UV−vis−NIR absorption spectrometer (Dunedin, FL). The size and morphology of the NPs were examined with a JEOL JEM-1200 EXII electron transmission microscope (TEM). Size distribution was calculated from about 150 NPs. Chemical components of the nanostructures were determined using energy-dispersive X-ray spectroscopy (EDX) on a Nova NanoSEM 650 Field emission scanning electron microscope (FE-SEM). The magnetic properties were measured using a vibration sample magnetometer (Dexing Magnets, China). Magnetic separation was performed using a Qiagen 12-tube magnet with the surface field around 4000 G.

Determination of Photothermal Conversion Efficiency of IOC−Au NPCs. The photothermal conversion efficiency of the NPs was measured according to the method reported previously.[41,42] Specifically, 200 μL of 3.2 μg/mL IOC−Au NPCs (OD$_{808}$ = 1) in a 1.7 mL centrifuge vial was irradiated with a 808 nm diode laser (Power Technologies, Little Rock, AR). The diameter of the laser beam was 1 cm, and the power density was 0.55 W/cm^2. A thermocouple was inserted into the solution to record the temperature. The temperature was monitored during both heating (laser on) and cooling (laser off) stages. The photothermal conversion efficiency η was calculated using the following equation[41]

$$\eta = \frac{hS(T_{max} - T_{amb}) - Q_{dis}}{I(1 - 10^{-A_{808}})} \quad (1)$$

where h is the heat transfer coefficient, S is the surface area of the container, T_{max} is the maximum equilibrium temperature, T_{amb} is the ambient temperature of the surroundings, Q_{dis} is a parameter expressing the laser-induced heat input by the container, I is the laser power, and A_{808} is the absorbance of the NPs at 808 nm. The same experiment was conducted with water as the control to determine Q_{dis} (mW) by

$$Q_{dis} = 10^3 \cdot m \cdot C \cdot \Delta T / t \quad (2)$$

where m is the mass of water (g), C is the heat capacity of water (J g^{1-} K^{-1}), ΔT is the increased temperature (K), and t is the laser exposure time (s). The term hS was calculated based on

$$hS = \frac{\sum_i m_i C_{p,i}}{\tau_s} \quad (3)$$

where τ_s is the sample system time constant and i is the system components (NP suspension and sample container). τ_s is related to a dimensionless driving force temperature θ by

$$t = -\tau_s \ln \theta \quad (4)$$

where t is the cooling time and θ is given by

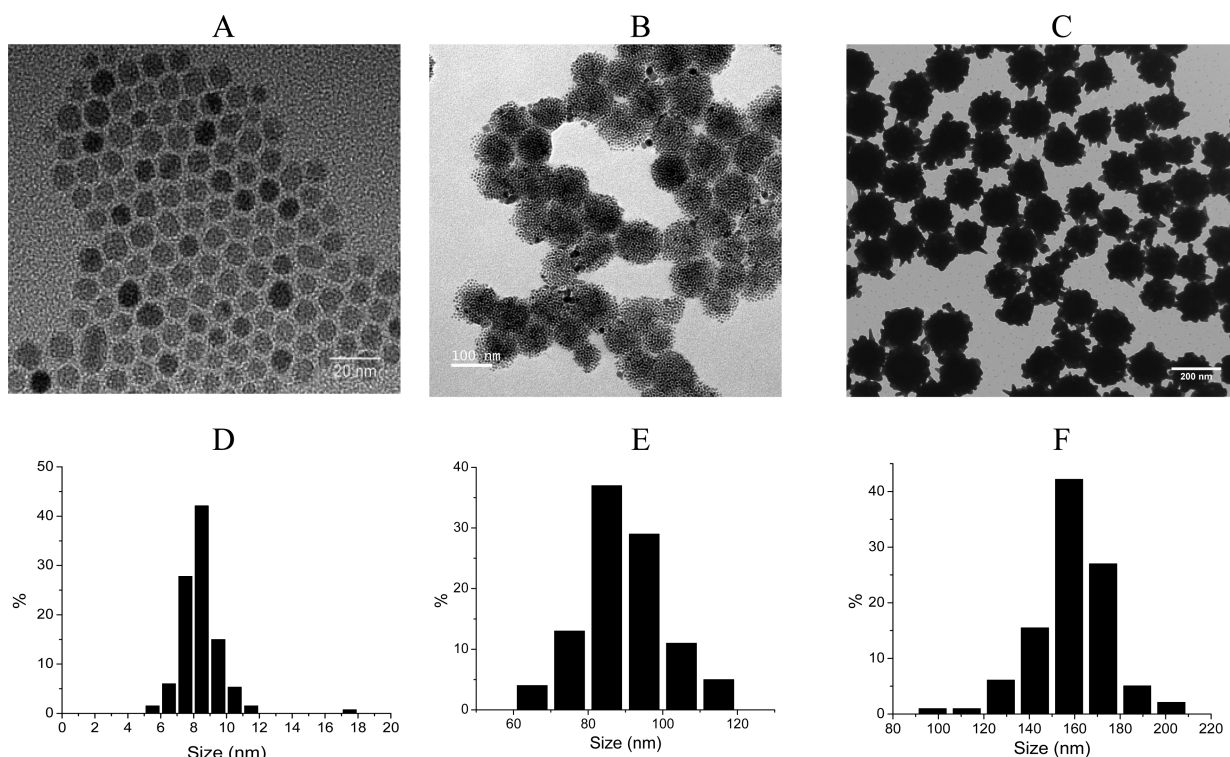$$\theta = (T - T_{amb})/(T_{max} - T_{amb}) \quad (5)$$

Figure 1. Structural characterization of IO NPs (A, D), IOCs (B, E) and IOC−Au NPCs (C, F). (A, B, C) TEM images. (D, E, F) Size distribution calculated from ~150 NPs. The average size of the IO NPs, IOCs, and IOC−Au NPCs was 8, 87, and 158 nm, respectively.

PS Loading and Stabilization on IOC−Au NPCs. PS loading and stabilization on the IOC−Au NPCs were performed by adapting our previously reported method.[43] First, 11-mercaptoundecanoic acid linked PEG (MUA-PEG) was synthesized as the stabilization agent. This was done through an N,N'-dicyclohexylcarbodiimide (DCC)-activated coupling reaction between PEG-NH$_2$ and MUA in anhydrous dichloromethane (DCM). The polymer was purified by centrifugal filtration. To load PS onto IOC−Au NPCs, 1 mL of 4.0 μg/mL IOC−Au NPCs was mixed with silicon 2,3-naphthalocyannie dihydroxide (SiNC) at various concentrations (0.05−4 μM) for 15 min. Then, 250 μL of 1 mM MUA-PEG was added and the solution was stirred for another 45 min. The MUA-PEG/SiNC/IOC−Au NPCs were purified by three rounds of centrifugation (12 000 rpm, 10 min) and washing with ultrapure water. The residue was reconstituted with ultrapure water. The nanocomplex with the saturated SiNC coating was used for further studies.

Stability of SiNC-Loaded IOC−Au NPCs in Phosphate Buffered Saline (PBS), Cell Culture Medium, and Serum. MUA-PEG/SiNC/IOC−Au NPCs were dispersed in 1 × PBS (pH 7.4, 137 mM NaCl, 2.7 mM KCl, 4.3 mM Na$_2$HPO$_4$ and 1.47 mM KH$_2$PO$_4$), RPMI 1640 cell culture medium (Mediatech, Inc., Manassas, VA) with 10% fetal bovine serum (FBS, Gemini Bio-Products, West Sacramento, CA) or 100% FBS to make 1 mL of 4 μg/mL solution. The solution was shaken on an orbital shaker (600 rpm) to mimic blood circulation. At a specified time from 30 to 360 min, 200 μL of the solution was withdrawn and centrifuged. The supernatant was collected and mixed with an equal volume of DCM and stirred vigorously for 4 h. Then, the DCM layer was collected and the solvent was evaporated. The residue was reconstituted and concentrated with 20 μL of DMSO. SiNC was quantified by Raman spectroscopy using a portable Raman spectrometer (Enwave Optronics, Inc., Irvine, CA).

SiNC Release from IOC−Au NPCs w/ and w/o Magnetic Attraction under Cellular Environment. KB-3-1 head and neck cancer cells were cultured in RPMI 1640 medium supplemented with 10% (v/v) FBS and pencilium−streptomycin solution (100 U/mL penicillin, 100 U/mL streptomycine) at 37 °C under 5% CO$_2$. The cells were seeded at a density of 8 × 10^3 cells per well into 96-well

plates in triplicate. After 24 h, the medium was replaced with 100 μL of fresh medium containing 4 μg/mL MUA-PEG/SiNC/IOC−Au NPCs. After a specified time from 30 to 360 min, the cell culture medium was collected. SiNC in the medium was extracted with DCM, followed by solvent evaporation and resuspension with DMSO. SiNC was quantified by Raman spectroscopy. SiNC released was expressed as the percentage of SiNC inside cells compared to the total amount of SiNC from the added MUA-PEG/SiNC/IOC−Au NPCs. The same experiment was performed in the presence of a magnetic field, in which a permanent neodymium−iron−boron (NdFeB) block magnet (4″ × 4″ × 2″ thick, surface field: ~4900 G) was paced under the 96-plate during incubation. To ensure the similar field for each well, only the cell wells located within a 2″ × 2″ area of the magnet were used.

Laser Irradiation, Magnetic Attraction, and Cell Viability Assay. KB-3-1 and SK-BR-3 (breast cancer) cells were seeded at a density of 8 × 10^3 cells per well into 96-well plates in triplicate. After 24 h, the medium was replaced with 100 μL of fresh medium containing the following formulations: (1) SiNC (DMSO as the solvent), (2) MUA-PEG/IOC−Au NPCs, (3) MUA-PEG/SiNC/IOC−Au NPCs, and (4) MUA-PEG/SiNC/IOC−Au NPCs w/ NdFeB block magnet. Cells w/o any treatment were used as the control. The laser treatment, 10 min irradiation with a 808 nm diode laser (Beam size: 8 mm. Power intensity: 0.55 W/cm^2) (Power Technologies, Little Rock, AR), was conducted 2 h after the addition of the formulations. After laser irradiation, cells were washed with PBS and incubated in drug-free medium for overnight. The effect of dosage on cell killing efficiency was examined by using different concentrations of the nanocomplex from 1 to 4 μg/mL. Free drug was added at an equivalent concentration of SiNC in the nanocomplex. Cell viability was determined using the XTT toxicology assay. The cell viability was expressed as the percentage of live cells over that of the untreated control. The data are presented as the mean ± standard deviation of triplicate measurements.

Statistical Analysis. The statistical significance of the cell viabilities under different treatments and different concentrations was compared using the analysis of variance (ANOVA). A P-value < 0.05 was considered statistically significant in all cases. Multiple comparison procedures were used after obtaining a significant
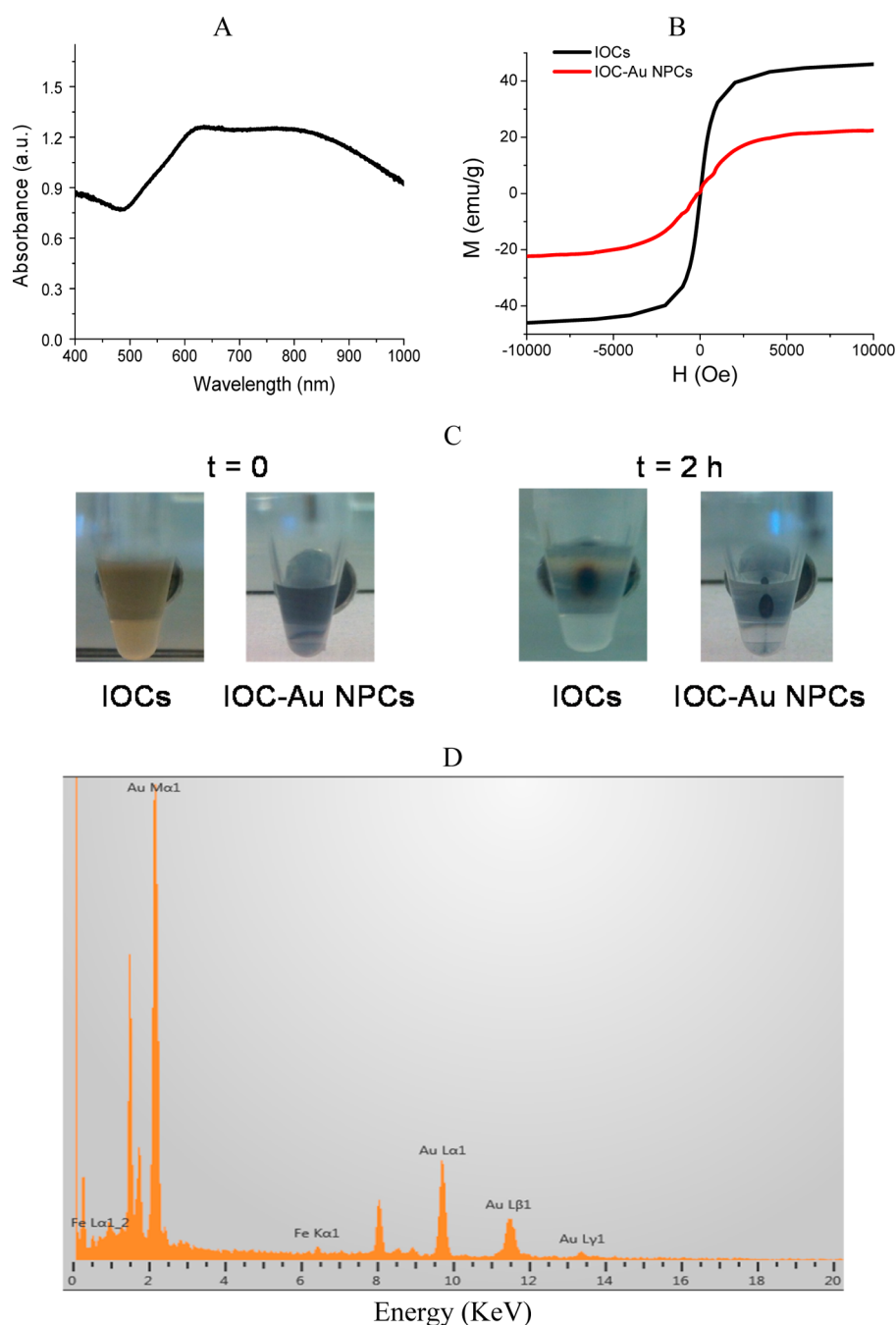
Figure 2. Optical absorption and magnetic properties of IOC−Au NPCs. (A) Absorption spectrum of IOC−Au NPCs. (B) Room-temperature magnetization curves of IOCs and IOC−Au NPCs. (C) Photographs of the magnetic separation of IOCs and IOC−Au NPCs. (D) EDX spectrum of IOC−Au NPCs.

ANOVA result. A post hoc Scheffe method was applied to determine which means differed. The mean difference between treatments or concentrations was considered to be significant if the absolute value was greater than the minimum significant difference (MSD) that was derived from the Scheffe method.

3. RESULTS AND DISCUSSION

Synthesis and Characterization of IOC−Au NPCs. NIR-absorbing Au NPs with an IO core have been previously made by several research groups, including our group.[40,44−53] In these studies, single IO NPs were used as the core materials. It will be highly desirable to make the hybrid NPs with an IOC core. This is because IOCs show better magnetic properties

compared to the individual IO NPs as each cluster is composed of many individual particles. For example, research has shown that IOCs (~100 nm in diameter) show 2 times higher T2 relaxivity coefficients than the individual IO NPs (~9 nm in diameter),[54] making them excellent contrast agents for magnetic resonance imaging (MRI).

Oleic acid coated IO NPs were prepared by the classic thermal decomposition method.[38] The NPs were about 8 ± 1.3 nm (mean ± SD) in diameter (Figure 1A,D). The IOCs were prepared by self-assembly of the IO NPs with alkyl-PEI2K. The low molecular weight amphiphilic polymer transfers hydrophobic IO NPs from organic solvent to aqueous phase while holding multiple particles together to form clustered structures.
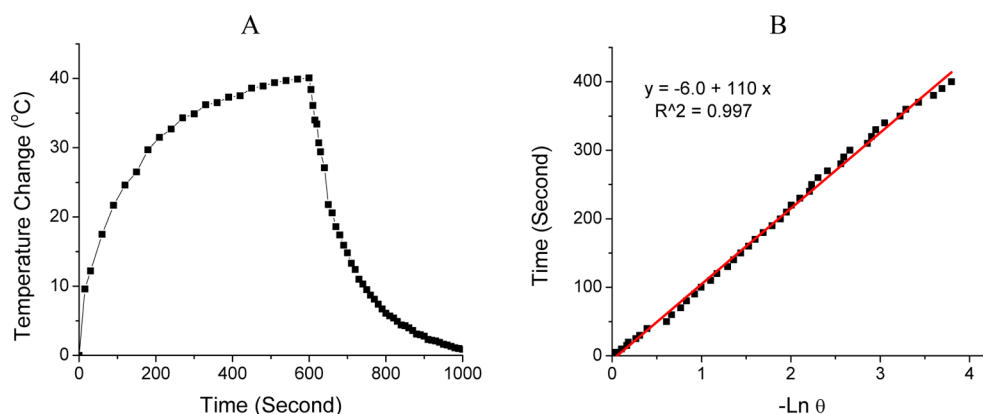
Figure 3. Photothermal property of IOC−Au NPCs. (A) Plot of the temperature vs time for the IO−Au NPCs (4.0 μg/mL, OD_{808} = 1.0) during laser irradiation (808 nm, 0.55 W/cm^2) and cooling (laser off). The temperature increased from an ambient value of 21.4 °C to an equilibrium value of 62.0 °C during continuous irradiation for 600 s. (B) Plot of the cooling time vs −ln θ. On the basis of the linear regression analysis, the time constant for heat transfer τ_s (the slope of the plot) was determined to be 110 s.

The diameter of the IOCs was 87 ± 11 nm (Figure 1B,E). The clusters were well dispersed in water and stable up to 6 months at room temperature.

In order to grow Au on the IOCs, the clusters were coated with PSS by electrostatic adsorption to introduce a negative charge through the sulfonate groups. These negatively charged groups were used as the anchor points to adsorb $Ag(NH_3)_2^+$ ions that were subsequently reduced to form small Ag NPs (2−5 nm) as the nucleation sites for the growth of the Au shell. PSS coating was confirmed by DLS characterization (Table S1, Supporting Information). The PSS-coated IOCs showed a surface potential of −19.8 mV, in contrast to the highly positive charge of the PEI-coated clusters (43.2 mV). The formation of IOC−Au NPs was initiated by injection of the Ag-adsorbed IOCs into a reduced Au growth solution containing $HAuCl_2$, CTAB, $AgNO_3$, and AA. Such a growth solution has been widely used to make metal NPs in various shapes by fine control of the concentration of the chemical components.[55,56] The formation of various shapes is the outcome of the interplay between the faceting binding tendency of the stabilizing agent CTAB and the growth kinetics.[55] Preparation of anisotropic nanostructures is desirable because anisotropic NPs are known to give better electric field enhancement than the spherical ones,[57] a phenomenon that enhances many optical activities such as surface enhanced Raman scattering (SERS). In our studies, we made IOC−Au NPCs with the reduced growth solution consisting of 0.4 mM $HAuCl_2$, 0.1 M CTAB, 80 μM $AgNO_3$, and 1.2 mM AA. TEM characterization showed that the IOC−Au NPCs were 158 ± 18 nm (Figure 1C,F). Considering the thickness of the PSS layer (∼10 nm determined by DLS), the average thickness of the external Au structure was about 30 nm.

The IOC−Au NPCs absorb in the NIR region, with a broad LSPR peak around 800 nm (Figure 2A). They are superparamagnetic, with a saturation magnetization around 22 emu/g (Figure 2B). This value is approximately one-half of that of the IOCs, due to the mass contribution from the diamagnetic Au that has a 4-fold higher density than the IO. The magnetic property was further confirmed by their separation in the presence of a magnetic field. The IOC−Au NPCs were separated from the solution within 2 h when the sample was attached to a permanent magnet, similar to the IOCs (Figure 2C). This demonstrates that the IOC−Au NPCs are indeed core−shell NPs. The EDX spectrum reveals the presence of

both Fe and Au (Figure 2D). The relative intensities of the Au and Fe peaks indicate that the particles are largely of Au character. In addition, Au has a much higher atomic weight than Fe, which also contributes to the strong signals from Au. The peak at 8 keV is from Cu on the support TEM grid.

To understand the growth mechanism of the hybrid NPs, we examined the effects of particle formation by the amount of Au precursor in the growth solution. This was done by injecting different amounts of the Ag-decorated IOC seed. The results showed that, when the amount of the seed was high (relative amount of Au precursor per seed particle is low), individual Au NPs on the IOCs were clearly seen (Figure S1A, Supporting Information). When the amount of seed was decreased, the individual Au NPs grew larger and adjacent Au NPs coalesced by the deposition of Au onto the NPs from solution (Figure S1B−D). The LSPR band red-shifted in wavelength and increased in intensity (Figure S1F). When the amount of the seed was further decreased, IOC−Au NPs with protrudent Au structures formed, resulting in IOC−Au NPCs (Figure S1E). HRTEM images of individual NPs revealed that the Au grew along the (111) direction (Figure S2, Supporting Information).

Photothermal Performance of the IOC−Au NPCs. To investigate the potential capability of the IOC−Au NPCs for photothermal therapy, the photothermal conversion efficiency, η, of the particles was determined. In these studies, the temperature of an NP solution under continuous laser irradiation and subsequent cooling with the laser being turned off was recorded. The cooling process was used to determine the rate of heat transfer from the NP solution to the environment. Figure 3A shows the plot of the temperature versus time for an aqueous IOC−Au NPC sample (OD = 1.0) during the laser heating and cooling processes. The temperature increased by 40 °C when the NP solution was irradiated for 320 s and did not change significantly with further irradiation. The temperature reached a maximum because of the equilibrium between the heat input and output. In contrast, the temperature of the control water increased by only 0.9 °C (Figure S3, Supporting Information). Using eq 2 and the heating profile of the water, the Q_{dis} was determined to be 1.57 mW. Figure 3B shows the plot of the cooling time t versus the term −ln θ. The data shows a linear relationship, giving a slope of 110.6 s, the τ_s. Using eq 3, the term hS was calculated to be 7.6 mW/°C. On the basis of eq 1, the efficiency of transducing the red laser to heat by the IOC−Au NPCs was calculated to be

61%. For comparison, we made Au NRs, one of the well-known NIR-absorbing Au nanostructures in PTT. The NRs have an averaged aspect ratio of 4.1, with a length around 45 nm and a width around 11 nm (Figure S4A, Supporting Information). The NRs have the LSPR around 795 nm, largely overlapping with the NIR laser wavelength at 808 nm (Figure S4B). Figure S4C shows the plot of the temperature versus time for an aqueous Au NRs sample (OD_{808} = 1.0) during the laser heating and cooling processes. The plot of the cooling time t versus the term $-\ln \theta$ is shown in Figure S4D. On the basis of this information and eqs 1−5, we determined that the photothermal conversion efficiency of Au NRs is 75%, which is higher than that of IO−Au NPCs. This is not surprising because photothermal conversion efficiency is largely dependent on the particle's volume, shape, and structure as well as the overlapping of the LSPR of the NPs with the laser wavelength.[58] Chen and co-workers recently reported that Au bellflowers around 150 nm show a photothermal conversion efficiency of 74% in the NIR region.[15] For NPs with a similar shape and structure, larger NPs have stronger light scattering contribution in the total extinction efficiency and thus may give lower photothermal conversion efficiencies than smaller NPs. It is worth to mention that other researchers have reported different photothermal conversion efficiencies of Au NRs (24%,[41] 60%,[59] and 90%[58]) depending on the dimension of the NRs and the laser source used. Under our experimental conditions, Au NRs show higher photothermal conversion efficiency and correspondingly work better than IO−Au NPCs in PTT. However, Au NRs do not have magnetic properties. The IO−Au hybrid NPCs have combined optical and magnetic properties and thus offer new capabilites in biomedical diagnostics and treatment.

Preparation and Characterization of SiNC-Loaded IOC−Au NPCs. To achieve deep light penetration into tissue, an ideal PS agent should absorb light in the NIR region. They should also have good singlet oxygen quantum yield ($\phi_\Delta \geq 0.2$) to ensure sufficient efficacy. Hydrophobic sensitizers are generally more effective than hydrophilic ones in cells and tumor uptake with a similar yield of singlet oxygen.[60] We chose SiNC as the PS agents. SiNC is one of the dye-based hydrophobic PS molecules. It has strong absorption in the NIR window, with the absorption maxima at 778 nm in DMSO (Figure 4). In a more hydrophilic environment (3DMSO:1 water), the absorption maxima is red-shifted to 795 nm, which
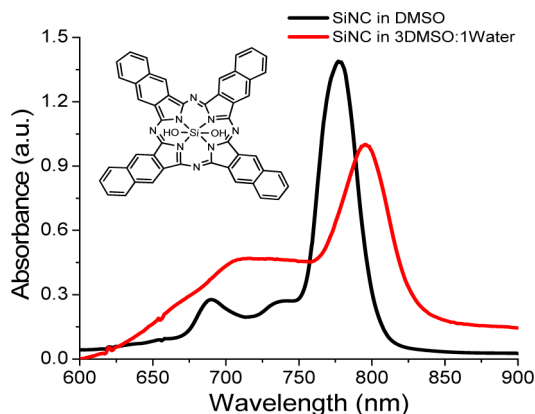
overlaps well with the irradiation laser wavelength (808 nm). The SiNC has a good singlet oxygen quantum yield (ϕ_Δ = 0.35),[61] comparable to that of the clinically used phthalocyanine (PC)-based molecules that has only marginal NIR absorption.[62]

We have previously demonstrated that a hydrophobic drug can be loaded onto Au nanorods through the interaction of the drug with the hydrophobic interior of the CTAB capping bilayer on the surface of the nanorods.[43] CTAB was then replaced with amphiphilic MUA-PEG without displacing the drug molecules. The drug was entrapped in the hydrophobic interior of the MUA-PEG monolayer. Using the same method, we loaded SiNC onto IOC−Au NPCs and stabilized the SiNC-adsorbed particles with MUA-PEG. The SiNC adsorption was characterized by SERS measurement. The MUA-PEG/SiNC/IOC−Au NPCs gave strong Raman signals from SiNC, indicating successful SiNC adsorption (Figure 5A). The signal intensity increased with the increase of the SiNC concentration, reaching a maximum around 1 μM due to saturated adsorption (Figure 5B). Assuming that all SiNC was adsorbed at this condition, the loading efficiency was 19.4% (mass of SiNC/mass of Fe). Subsequent MUA-PEG binding was examined by DLS measurement.

Table 1 showed that the as-prepared IOC−Au NPCs had the hydrodynamic diameter (HD) of 170 nm and zeta potential (ξ) of +27 mV. The highly positive surface charge is due to the positively charged CTAB capping materials. When the particles were modified with MUA-PEG (w/ or w/o SiNC), the HD of the NPCs increased by 20 nm and the ξ decreased by 35 mV. These changes indicate the successfully replacement of CTAB by MUA-PEG on the surface of the particles.

Stability and Drug Release Profile of MUA-PEG/SiNC/IOC−Au NPCs. The stability of the nanocomplex was examined in PBS, cell culture medium, and 100% serum. To mimic blood circulation, the nanocomplexes in the above solutions were continuously shaken on an orbital shaker. At different times, an aliquot of the solution was centrifuged and the supernatant was extracted with DCM to determine the amount of SiNC released from the nanocomplex. SiNC was quantified by Raman spectroscopy. Although SiNC gave weaker Raman signals than those adsorbed on the particles, quantization of SiNC can be achieved at elevated laser power and acquisition time (Figure S5, Supporting Information). Figure 6A shows that less than 2% of SiNC was released after 1 h in all the solutions. After 6 h, less than 8% of SiNC was released in all cases. These results demonstrate that the MUA-PEG/SiNC/IOC−Au NPCs have excellent stability in the physiological environments. The SiNC release property was studied under a cellular environment. In this study, we incubated SK-BR-3 cells with cell culture medium containing MUA-PEG/SiNC/IOC−Au NPCs. After a specified time, we determined the amount of SiNC remaining in the medium. We assumed that all the SiNC released from the nanocomplex entered cells. Figure 6B (black) shows that the nanocomplex exhibits a biphasic drug release profile with the rapid release process occurring within the first 2 h. Then, SiNC release slowly increased, with 78% of SiNC released at 5 h. These studies demonstrate that SiNC release from the MUA-PEG/SiNC/IOC−Au NPCs is highly efficient upon exposure to live cells. The release is due to the preferential localization of hydrophobic drugs to the cell lipid membrane.[43]

A similar study was performed in the presence of a magnetic field. In this experiment, a permanent magnet (surface field ∼

Figure 4. Structure (inset) and absorption spectra of SiNC. The absorption maximum is 778 nm in DMSO and 795 nm in DMSO/water.
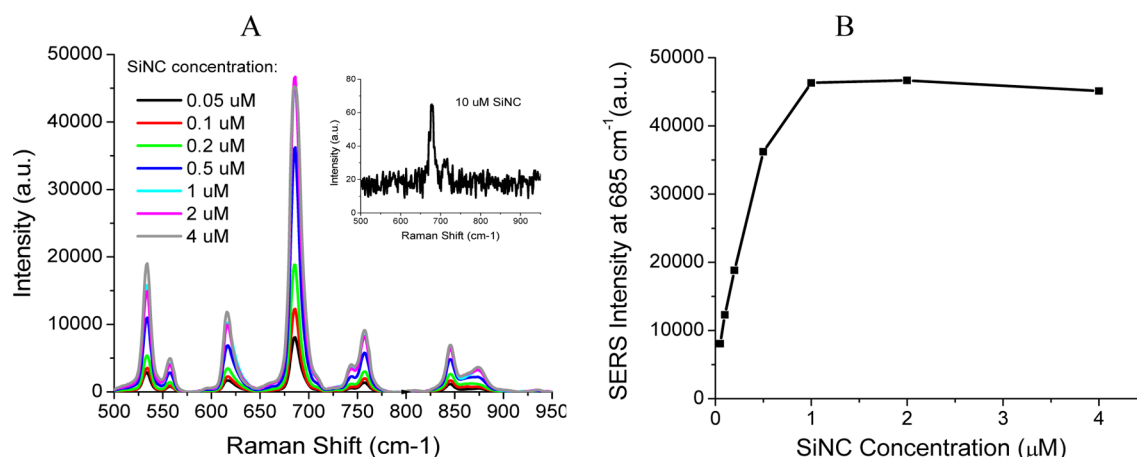
Figure 5. Characterization of SiNC loading onto IOC−Au NPCs by SERS spectroscopy. (A) SERS spectra of MUA-PEG/SiNC/IOC−Au NPCs at different SiNC loading concentrations. (B) Plot of SERS signal intensity at 685 cm^{-1} vs the SiNC loading concentration. Excitation laser wavelength: 785 nm. Laser power: 25 mW. Acquisition time: 1 s.

Table 1. Characterization of SiNC Loading onto IOC−Au NPCs by Dynamic Light Scattering Method

	HD (nm)	ξ (mV)
IOC−Au NPCs	170.4 ± 3.4	27 ± 1.3
MUA-PEG/IOC−Au NPCs	189.7 ± 2.8	−7.2 ± 0.8
MUA-PEG/SiNC/IOC−Au NPCs	190.2 ± 2.7	−7.8 ± 1.0

4900 G) was placed under the 96-well plate during the incubation. Figure 6B (red) shows that the SiNC release profile w/ the magnetic field is similar to those w/o the magnetic field. However, the release efficiency at each examined time point is relatively higher. For examples, at 30 min, while 37% SiNC was released from the nanocomplex w/o the magnetic field, 52% SiNC was released w/ the magnetic field. At 2 h, SiNC release was 65% and 81% for w/o and w/ the magnetic field, respectively. This indicates that the magnetic field significantly accelerated the release of SiNC. This is because the magnetic field facilitates the movement of the magnetic nanocomplex toward the cell membrane. With further incubation (>10 h), however, the amount of SiNC released w/ the magnetic field is only slightly higher than that w/o the magnetic field. This is not surprising since the majority of loaded SiNC has been released within 10 h. It is realized that, under *in vivo* conditions,

magnetic attraction will not only accelerate SiNC release but also enhance deep penetration of the nanocarrier and the cargos.[37]

Photothermal and Photodynamic Therapy w/ and w/ o Magnetic-Field-Guided Drug Delivery. To examine the capabilities of the nanocomplexes for dual mode PTT and PDT as well as the effect of magnetic-field-guided drug delivery on the therapeutic efficacy, we comparably studied the cytotoxic effects of PTT, PDT, PTT + PDT, and PTT + PDT + magnetic attraction using MUA-PEG/IOC−Au NPCs, SiNC, MUA-PEG/SiNC/IOC−Au NPCs, and MUA-PEG/SiNC/ IOC−Au NPCs w/ magnetic attraction, respectively. In these studies, cells were incubated with the above drug formulations for 2 h and then subjected to laser irradiation for 10 min. The concentration of SiNC used for the PDT treatment in each dose was determined based on the SiNC loading efficiency and the release efficiency at 2 h w/o the magnet (see Figure 6). For these samples with a magnetic field, the magnet was placed under the cell culture before the addition of drug formulations and remained under the plates during the whole course of experiments. After laser treatment (10 min, 0.55 W/cm^2), the cells were washed three times with PBS to remove drugs and then incubated in drug-free medium for overnight before the
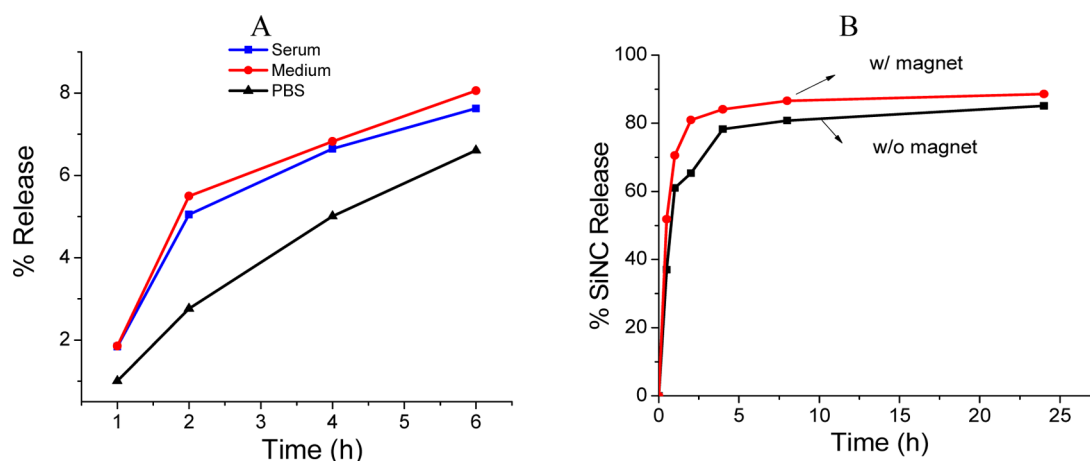

Figure 6. Stability (A) and drug release profile (B) of MUA-PEG/SiNC/IOC−Au NPCs. Drug release in (B) were determined under a cellular environment. w/: with. w/o: without.

XTT assay. The studies were carried out using two different cell lines KB-3-1 and SK-BR-3 under three different doses 1, 2, and 4 μg/mL nanocomplex or free SiNC with equivalent concentrations.

Figure 7 shows the cell viabilities under different treatments at three doses. Statistical analysis with ANOVA, followed by
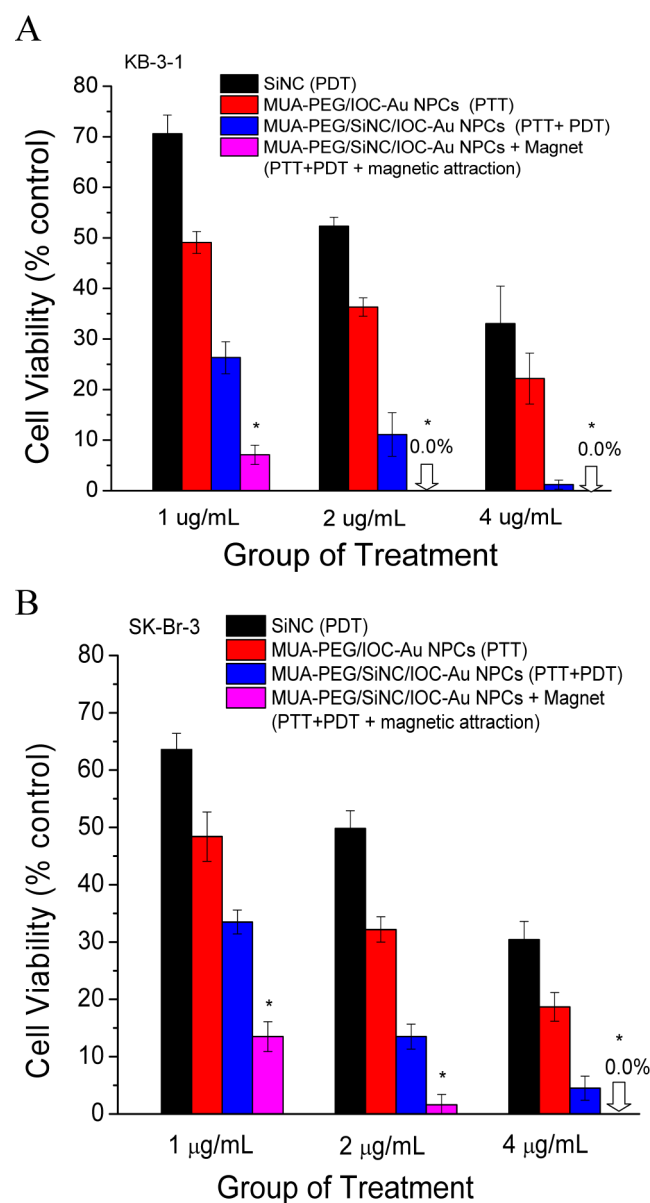

Figure 7. Comparison of the efficacy of PTT + PDT + magnetic attraction against KB-3-1 (A) and SK-BR-3 (B) cells to that of PTT, PDT, and PTT + PDT. PTT, PDT, and PDT + PTT were achieved using MUA-PEG/IOC−Au NPCs, SiNC, and MUA-PEG/SiNC/IOC−Au NPCs, respectively. The results are mean values ± SD of triplicate experiments. (*$P < 0.05$ as compared to PTT, PDT, and PTT + PDT).

pairwise comparisons using the Scheffe method, showed significant differences ($P < 0.05$, Mean difference > MSD) between the different groups (Tables S2−S7, Supporting Information). These differences were reproducible in both cell lines and at multiple dosages. For example, when the KB-3-1 cells were treated with a low concentration (1 μg/mL) of MUA-PEG/IO−Au NPCs and laser irradiation (PTT), 49.1%

cells remained alive. When the cells were treated with an equivalent concentration of SiNC (0.19 μg/mL) and laser irradiation (PDT), 70.9% cells remained alive. However, when the cells were treated with 1 μg/mL MUA-PEG/SiNC/IO−Au NPCs and laser irradiation (PTT + PDT), the cell viability was reduced to 26.3%. The cell viability was further reduced to 7.1% with the use of magnetic attraction. These results showed that the combination treatment killed 23% more cells than PTT and 45% more cells than PDT. Using magnetic attraction, the combination treatment killed 42% more cells than PTT and 64% more cells than PDT. The enhanced efficacy with the use of magnetic attraction is attributed to the increased amount of PDT inside the cells, as shown in Figure 6B. It is worthy to mention that the temperature of the medium was only raised to 42−45 °C when PTT was involved. These studies demonstrate that combined PTT and PDT using MUA-PEG/SiNC/IO−Au NPCs are much more effective than PTT or PDT alone. The magnetic attraction further amplified the combination treatment at a large degree, due to increased cellular uptake of the PS agents as the field facilitated the movement of the nanocomplex toward cell membrane.

Increasing the concentration of the drug formulations led to increased cell killing for all treatment groups. For the combination group, the cell viability was decreased to 11.1% at 2 μg/mL and 1.2% at 4 μg/mL MUA-PEG/SiNC/IO−Au NPCs in KB-3-1 cells. A similar trend was observed in SK-BR-3 cells. When the magnetic field was used, all KB-3-1 cells were killed at both 2 and 4 μg/mL MUA-PEG/SiNC/IO−Au NPCs and all SK-BR-3 cells were killed at 4 μg/mL MUA-PEG/SiNC/IO−Au NPCs. The temperature of the medium in the presence of 2 and 4 μg/mL MUA-PEG/SiNC/IO−Au NPCs was raised to 55 and 62 °C, respectively. These studies demonstrate that highly efficient cell killing can be achieved with a low dose of drug formulations ($\leq$4 μg(Fe)/mL) and low intensity of laser (0.55 W/cm^2) under the combinatorial PTT and PDT with the assistance of magnetic-field-guided drug delivery using the MUA-PEG/SiNC/IO−Au NPC complex.

Synergistic/Additive Effects of the Combination Treatment. Thermal effect could increase cell membrane permeability, thus increasing drug diffusion. It could also change the drug uptake kinetics. These factors may lead to a synergistic effect between PTT and PDT, amplifying the therapeutic outcome. To determine whether a synergist effect exists in the combination treatment in our system, cell viability was compared to a purely additive result from PTT and PDT. The additive result was calculated according to the following relationship[63]

$$f_{additive} = f_{PTT} \times f_{PDT} \qquad (6)$$

where $f_{additive}$ is the fraction of surviving cells by additive interaction of PTT and PDT, f_{PTT} is the fraction of surviving cells resulting from PTT treatment, and f_{PDT} is the fraction of surviving cells resulting from PDT. When the fraction of surviving cells from the combination treatment, $f_{combination}$, is lower than $f_{additive}$, there is a synergistic effect between the two treatments. When $f_{combination} = f_{additive}$, there is an additive effect. When $f_{combination}$ is larger than $f_{additive}$, there is an antagonistic effect. The calculated $f_{additive}$ in both cell lines is listed in Table 2. The results showed that the $f_{combination}$ of PDT and PTT was significantly lower than the calculated $f_{additive}$ in KB-3-1 cells in all three doses, indicating a synergist effect between PTT and PDT in this cell line. However, no significant difference between $f_{combination}$ and $f_{additive}$ of PDT and PTT was observed in

Table 2. Comparison of Calculated $f_{additive}$ from PDT and PTT with Experimental $f_{combination}$ for PTT + PDT and PTT + PDT + Magnetic Attraction

cell line	MUA-PEG/SiNC/IOC-Au NPC concentration (μg(Fe)/mL)	$f_{additive\ (PTT + PDT)}$ (%)	$f_{combination\ (PTT + PDT)}$ (%)	$f_{combination\ (PTT + PDT + magnetic\ attraction)}$ (%)
KB-3-1	1	34.7	26.3	7.1
	2	19.0	11.1	0.0
	4	7.3	1.2	0.0
SK-BR-3	1	30.7	33.5	13.5
	2	16.0	13.5	1.6
	4	5.7	4.5	0.0

the SK-BR-3 cells, indicating an additive effect between these two treatments in this cell line. The PTT + PDT + magnetic attraction gave lower $f_{combination}$ values than those from PTT + PDT, due to the increased concentration of SiNC inside cells via the magnetic attraction.

4. CONCLUSION

We have synthesized popcorn-shaped dual functional iron oxide–gold nanostructures and demonstrated their capability for magnetic-field-guided drug delivery and combinatorial PTT and PDT for cancer. The hybrid nanostructures were prepared via seed-mediated growth of Au onto self-assembled IO clusters. They are superparamagnetic and NIR-responsive, with excellent photothermal conversion efficiency. A stable and compact nanocomplex for dual PTT and PDT was formed using the hybrid nanostructures as the PS carriers and PT agents, NIR-absorbing SiNC as the PS agents, and MUA-PEG as the stabilization agents. PS release and intracellular uptake was enhanced by applying a magnetic field. Combined PTT and PDT in conjunction with magnetic-field-assisted drug delivery using the nanocomplex was demonstrated to be highly effective, leading to complete eradication of cultured cancer cells *in vitro* at a dose of 2 μg(Fe)/mL nanocomplex for KB-3-1 cells and 4 μg(Fe)/mL for SK-BR-3 cells with low intensity of NIR light (0.55 W/cm^2). We expect that the novel nanocomplex will be able to deliver a high concentration of PS molecules and the nanocarriers deep into tumor tissue via applying a magnetic field on the surface of tumors. The high concentration therapeutic agents, together with the excellent photothermal conversion efficiency of the hybrid nanostructures, would lead to highly effective tumor ablation via combined PTT and PDT. The all-in-one nanoplatform may prevent tumor regrowth and metastasis and have an important impact on the treatment of head and neck cancer, breast cancer, and other malignancies.

ASSOCIATED CONTENT

Ⓢ Supporting Information

Additional characterization of IOC–Au NPCs, laser heating profile of water, linearity of SiNC Raman signals, and statistical data of different types of treatments are available in the Supporting Information. The Supporting Information is available free of charge on the ACS Publications website at DOI: 10.1021/acsami.5b02741.

AUTHOR INFORMATION

Corresponding Authors

*E-mail: gangliu.cmitm@xmu.edu.cn (G. Liu).

*E-mail: xhuang4@memphis.edu (X. Huang).

Present Address

$\perp$Department of Chemical Engineering, Louisiana State University, Baton Rouge, LA 70803.

Author Contributions

$\parallel$These authors contributed equally.

Notes

The authors declare no competing financial interest.

REFERENCES

(1) Kennedy, L. C.; Bickford, L. R.; Lewinski, N. A.; Coughlin, A. J.; Hu, Y.; Day, E. S.; West, J. L.; Drezek, R. A. A New Era for Cancer Treatment: Gold-Nanoparticle-Mediated Thermal Therapies. *Small* **2011**, *7*, 169−183.

(2) Link, S.; El-Sayed, M. A. Shape and Size Dependence of Radiative, Non-radiative and Photothermal Properties of Gold Nanocrystals. *Int. Rev. Phys. Chem.* **2000**, *19*, 409−453.

(3) Hirsch, L. R.; Stafford, R. J.; Bankson, J. A.; Sershen, S. R.; Price, R. E.; Hazle, J. D.; Halas, N. J.; West, J. L. Nanoshell-Mediated Near Infrared Thermal Therapy of Tumors under MR Guidance. *Proc. Natl. Acad. Sci. U.S.A.* **2003**, *100*, 13549−13554.

(4) O'Neal, D. P.; Hirsch, L. R.; Halas, N. J.; Payne, J. D.; West, J. L. Photothermal Tumor Ablation in Mice Using Near Infrared Absorbing Nanoshells. *Cancer Lett.* **2004**, *209*, 171−176.

(5) Loo, C.; Lowery, A.; Halas, N. J.; West, J. L.; Drezek, R. Immunotargeted Nanoshells for Integrated Cancer Imaging and Therapy. *Nano Lett.* **2005**, *5*, 709−711.

(6) Huang, X.; El-Sayed, I. H.; Qian, W.; El-Sayed, M. A. Cancer Cell Imaging and Photothermal Therapy in the Near-Infrared Region by Using Gold Nanorods. *J. Am. Chem. Soc.* **2006**, *128*, 2115−2120.

(7) Tong, L.; Zhao, Y.; Huff, T. B.; Hansen, M. N.; Wei, A.; Cheng, J. X. Gold Nanorods Mediate Tumor Cell Death by Compromising Membrane Integrity. *Adv. Mater.* **2007**, *19*, 3136−3141.

(8) Dickerson, E. B.; Dreaden, E. C.; Huang, X.; El-Sayed, I. H.; Chu, H.; Pushpanketh, S.; McDonald, J. F.; El-Sayed, M. A. Gold Nanorod Assisted Near-Infrared Plasmonic Photothermal Therapy (PPTT) of Squamous Cell Carcinoma in Mice. *Cancer Lett.* **2008**, *269*, 57−66.

(9) von Maltzahn, G.; Park, J. H.; Agrawal, A.; Bandaru, N. K.; Das, S. K.; Sailor, M. J.; Bhatia, S. N. Computationally Guided Photothermal

Tumor Therapy Using Long-Circulating Gold Nanorod Antennas. *Cancer Res.* **2009**, *69*, 3892−3900.

(10) Chen, J.; Wang, D.; Xi, J.; Au, L.; Siekkinen, A.; Warsen, A.; Li, Z. Y.; Zhang, H.; Xia, Y.; Li, X. Immuno Gold Nanocages with Tailored Optical Properties for Targeted Photothermal Destruction of Cancer Cells. *Nano Lett.* **2007**, *7*, 1318−1322.

(11) Chen, J.; Glaus, C.; Laforest, R.; Zhang, Q.; Yang, M.; Gidding, M.; Welch, M. J.; Xia, Y. Gold Nanocages as Photothermal Transducers for Cancer Treatment. *Small* **2010**, *6*, 811−817.

(12) Melancon, M. P.; Lu, W.; Yang, Z.; Zhang, R.; Cheng, Z.; Elliot, A. M.; Stafford, J.; Olson, T.; Zhang, J. Z.; Li, C. In Vitro and in Vivo Targeting of Hollow Gold Nanoshells Directed at Epidermal Growth Factor Receptor for Photothermal Ablation Therapy. *Mol. Cancer Ther.* **2008**, *7*, 1730−1739.

(13) Lu, W.; Xiong, C.; Zhang, G.; Huang, Q.; Zhang, R.; Zhang, J. Z.; Li, C. Targeted Photothermal Ablation of Murine Melanomas with Melanocyte-Stimulating Hormone Analog Conjugated Hollow Gold Nanospheres. *Clin. Cancer Res.* **2009**, *15*, 876−886.

(14) Lu, W.; Singh, A. K.; Khan, S. A.; Senapati, D.; Yu, H.; Ray, P. C. Gold Nano-Popcorn-Based Targeted Diagnosis, Nanotherapy Treatment, and in Situ Monitoring of Photothermal Therapy Response of Prostate Cancer Cells Using Surface-Enhanced Raman Spectroscopy. *J. Am. Chem. Soc.* **2010**, *132*, 18103−18114.

(15) Huang, P.; Rong, P.; Lin, J.; Li, W.; Yan, X.; Zhang, M. G.; Nie, L.; Niu, G.; Lu, J.; Wang, W.; Chen, X. Triphase Interface Synthesis of Plasmonic Gold Bellflowers as Near-Infrared Light Mediated Acoustic and Thermal Theranostics. *J. Am. Chem. Soc.* **2014**, *136*, 8307−8313.

(16) Jain, P. K.; Lee, K. S.; El-Sayed, I. H.; El-Sayed, M. A. Calculated Absorption and Scattering Properties of Gold Nanoparticles of Different Size, Shape, and Composition: Applications in Biological Imaging and Biomedicine. *J. Phys. Chem. B* **2006**, *110*, 7238−7248.

(17) James, W. D.; Hirsch, L. R.; West, J. L.; O'Neal, P. D.; Payne, J. D. Application of INAA to the Build-Up and Clearance of Gold Nanoshells in Clinical Studies in Mice. *J. Radioanal. Nucl. Chem.* **2007**, *271*, 455−459.

(18) Huang, X.; Peng, X.; Wang, Y.; Wang, X.; Shin, D. M.; El-Sayed, M. A.; Nie, S. A Reexamination of Active and Passive Tumor Targeting by Using Rod-Shaped Gold Nanocrystals and Covalently Conjugated Peptide Ligands. *ACS Nano* **2010**, *4*, 5887−5896.

(19) Dougherty, T. J.; Gomer, C. J.; Henderson, B. W. Photodynamic Therapy. *J. Natl. Cancer Inst.* **1998**, *90*, 889−905.

(20) Robertson, C. A.; Evans, D. H.; Abrahamse, H. Photodynamic Therapy (PDT): A Short Review on Cellular Mechanisms and Cancer Research Applications for PDT. *J. Photochem. Photobiol., B* **2009**, *96*, 1−8.

(21) Celli, J. P.; Spring, B. Q.; Rizvi, I.; Evans, C. L.; Samkoe, K. S.; Verma, S.; Pogue, B. W.; Hasan, T. Imaging and Photodynamic Therapy: Mechanisms, Monitoring, and Optimization. *Chem. Rev.* **2010**, *110*, 2795−2838.

(22) van Nostrum, C. F. Polymeric Micelles to Deliver Photosensitizers for Photodynamic Therapy. *Adv. Drug Delivery Rev.* **2004**, *56*, 9−16.

(23) Chatterjee, D. K.; Fong, L. S.; Zhang, Y. Nanoparticles in Photodynamic Therapy: An Emerging Paradigm. *Adv. Drug Delivery Rev.* **2008**, *60*, 1627−1637.

(24) Olivo, M.; Bhuvaneswari, R.; Lucky, S. S.; Dendukuri, N.; Thong, P. S. P. Targeted Therapy of Cancer Using Photodynamic Therapy in Combination with Multi-faceted Anti-tumor Modalities. *Pharmaceuticals* **2010**, *3*, 1507−1529.

(25) Paszko, E.; Ehrhardtb, C.; Senge, M. O.; Kelleher, D. P.; Reynolds, J. V. Nanodrug Applications in Photodynamic Therapy. *Photodiagn. Photodyn. Ther.* **2011**, *8*, 14−29.

(26) Kah, J. C. Y.; Wan, R. C. Y.; Wong, K. Y.; Mhaisalkar, S.; Sheppard, C. J. R.; Olivo, M. Combinatorial Treatment of Photothermal Therapy Using Gold Nanoshells with Conventional Photodynamic Therapy To Imporve Treatment Effifacy: An In Vitro Study. *Lasers Surg. Med.* **2008**, *40*, 584−589.

(27) Kuo, W. S.; Chang, C. N.; Chang, Y. T.; Yang, M. H.; Chien, Y. H.; Chen, S. J.; Yeh, C. S. Gold Nanorods in Photodynamic Therapy,

as Hyperthermia Agents, and in Near-Infrared Optical Imaging. *Angew. Chem., Int. Ed* **2010**, *49*, 2711−2715.

(28) Tian, B.; Wang, C.; Zhang, S.; Feng, L.; Liu, Z. Photothermally Enhanced Photodynamic Therapy Delivered by Nano-Graphene Oxide. *ACS Nano* **2011**, *5*, 7000−7009.

(29) Jang, B.; Park, J. Y.; Tung, C. H.; Kim, I. H.; Choi, Y. Gold Nanorod-Photosensitizer Complex for Near-Infrared Fluorescence Imaging and Photodynamic/Photothermal Therapy In Vivo. *ACS Nano* **2011**, *5*, 1086−094.

(30) Kuo, W. S.; Chang, Y. T.; Cho, K. C.; Chiu, K. C.; Lien, C. H.; Yeh, C. S.; Chen, S. J. Gold Nanomaterials Conjugated with Indocyanine Green for Dual-Modality Photodynamic and Photothermal Therapy. *Biomaterials* **2012**, *33*, 3270−3278.

(31) Kim, J. Y.; Choi, W. I.; Kim, M.; Tae, G. Tumor-Targeting Nanogel That Can Function Independently for Both Photodynamic and Photothermal Therapy and Its Synergy from the Procedure of PDT Followed by PTT. *J. Controlled Release* **2013**, *171*, 113−121.

(32) Wang, J.; You, M.; Zhu, G.; Shukoor, M. I.; Chen, Z.; Zhao, Z.; Altman, M. B.; Yuan, Q.; Zhu, Z.; Chen, Y.; Huang, C. Z.; Tan, W. Photosensitizer-Gold Nanorod Composite for Targeted Multimodal Therapy. *Small* **2013**, *9*, 3678−3684.

(33) Sahu, A.; Choi, W. I.; Lee, J. H.; Tae, G. Graphene Oxide Mediated Delivery of Methylene Blue for Combined Photodynamic and Photothermal Therapy. *Biomaterials* **2013**, *34*, 6239−6248.

(34) Wang, Y.; Wang, H.; Liu, D.; Song, S.; Wang, X.; Zhang, H. Graphene Oxide Covalently Grafted Upconversion Nanoparticles for Combined NIR Mediated Imaging and Photothermal/Photodynamic Cancer Therapy. *Biomaterials* **2013**, *34*, 7715−7724.

(35) Peng, J.; Zhao, L.; Zhu, X.; Sun, Y.; Feng, W.; Gao, Y.; Wang, L.; Li, F. Hollow Silica Nanoparticles Loaded with Hydrophobic Phthalocyanine for Near-Infrared Photodynamic and Photothermal Combination Therapy. *Biomaterials* **2013**, *34*, 7905−7912.

(36) Chen, R.; Wang, X.; Yao, X.; Zheng, X.; Wang, J.; Jiang, X. Near-IR-Triggered Photothermal/Photodynamic Dual-Modality Therapy System via Chitosan Hybrid Nanospheres. *Biomaterials* **2013**, *34*, 8314−8322.

(37) Kong, S. D.; Zhang, W.; Lee, J. H.; Brammer, K.; Lal, R.; Karin, M.; Jin, S. Magnetically Vectored Nanocapsules for Tumor Penetration and Remotely Switchable On-Demand Drug Release. *Nano Lett.* **2010**, *10*, 5088−5092.

(38) Sun, S.; Zeng, H.; Robinson, D. B.; Raoux, S.; Rice, P. M.; Wang, S. X.; Li, G. Monodisperse MFe_2O_4 (M) Fe, Co, Mn) Nanoparticles. *J. Am. Chem. Soc.* **2004**, *126*, 273−279.

(39) Liu, G.; Wang, Z.; Lu, J.; Xia, C.; Gao, F.; Gong, Q.; Song, B.; Zhao, X.; Shuai, X.; Chen, X.; Ai, H.; Gu, Z. Low Molecular Weight Alkyl-Polycation Wrapped Magnetite Nanoparticle Clusters as MRI Probes for Stem Cell Labeling and In Vivo Imaging. *Biomaterials* **2011**, *32*, 528−537.

(40) Bhana, S.; Rai, B. K.; Mishra, S. R.; Wang, Y.; Huang, X. Synthesis and Properties of Near Infrared-Absorbing Magnetic-optical Nanopins. *Nanoscale* **2012**, *4*, 4939−4942.

(41) Tian, Q.; Jiang, F.; Zou, R.; Liu, Q.; Chen, Z.; Zhu, M.; Yang, S.; Wang, J.; Wang, J.; Hu, J. Hydrophilic Cu_9S_5 Nanocrystals: A Photothermal Agent with a 25.7% Heat Conversion Efficiency for Photothermal Ablation of Cancer Cells in Vivo. *ACS Nano* **2011**, *5*, 9761−9771.

(42) Roper, D. K.; Ahn, W.; Hoepfner, M. Microscale Heat Transfer Transduced by Surface Plasmon Resonant Gold Nanoparticles. *J. Phys. Chem. C* **2007**, *111*, 3636−3641.

(43) Ren, F.; Bhana, S.; Norman, D. D.; Johnson, J.; Xu, L.; Baker, D. L.; Parrill, A. L.; Huang, X. Gold Nanorods Carrying Paclitaxel for Photothermal-Chemotherapy of Cancer. *Bioconjugate Chem.* **2013**, *24*, 376−386.

(44) Salgueiriño-Maceira, V.; Correa-Duarte, M. A.; Farle, M.; López-Quintela, A.; Sieradzki, K.; Diaz, R. Bifunctional Gold-Coated Magnetic Silica Spheres. *Chem. Mater.* **2006**, *18*, 2701−2706.

(45) Wang, H.; Brandl, D. W.; Le, F.; Nordlander, P.; Halas, N. J. Nanorice: A Hybrid Plasmonic Nanostructure. *Nano Lett.* **2006**, *6*, 827−832.

(46) Ji, X.; Shao, R.; Elliott, A. M.; Stafford, R. J.; Esparza-Coss, E.; Bankson, J. A.; Liang, G.; Luo, Z. P.; Park, K.; Markert, J. T.; Li, C. Bifunctional Gold Nanoshells with a Superparamagnetic Ion Oxide-Silica Core Suitable for Both MR Imaging and Photothermal Therapy. *J. Phys. Chem. C* **2007**, *111*, 6245−6251.

(47) Wang, L.; Bai, J.; Li, Y.; Huang, Y. Multifunctional Nanoparticles Displaying Magnetization and Near-IR Absorption. *Angew. Chem., Int. Ed.* **2008**, *47*, 2439−2442.

(48) Wei, Q.; Song, H. M.; Leonov, A. P.; Hale, J. A.; Oh, D.; Ong, Q. K.; Ritchie, K.; Wei, A. Gyromagnetic Imaging: Dynamic Optical Contrast Using Gold Nanostars with Magnetic Cores. *J. Am. Chem. Soc.* **2009**, *131*, 9728−9734.

(49) Ma, L. L.; Feldman, M. D.; Tam, J. M.; Paranjape, A. S.; Cheruku, K. K.; Larson, T. A.; Tam, J. O.; Ingram, D. R.; Paramita, V.; Villard, J. W.; Jenkins, J. T.; Wang, T.; Clarke, G. D.; Asmis, R.; Sokolov, K.; Chandrasekar, B.; Milner, T. E.; Johnston, K. P. Small Multifunctional Nanoclusters (nanoroses) for Targeted Cellular Imaging and Therapy. *ACS Nano* **2009**, *3*, 2686−2696.

(50) Song, H. M.; Wei, Q.; Ong, Q. K.; Wei, A. Plasmon-Resonant Nanoparticles and Nanostars with Magnetic Cores: Synthesis and Magnetomotive Imaging. *ACS Nano* **2010**, *4*, 5163−5173.

(51) Jin, Y.; Jia, C.; Huang, S. W.; O'Donnel, M.; Gao, X. Multifuncional Nanoparticles as Coupled Contrast Agents. *Nat. Commun.* **2010**, *1*, 1−8.

(52) Fan, Z.; Shelton, M.; Singh, A. K.; Senapati, D.; Khan, S. A.; Ray, P. C. Multifunctional Plasmonic Shell−Magnetic Core Nanoparticles for Targeted Diagnostics, Isolation, and Photothermal Destruction of Tumor Cells. *ACS Nano* **2012**, *6*, 1065−1073.

(53) Zhang, Q.; Ge, J.; Goebl, J.; Hu, Y.; Sun, Y.; Yin, Y. Tailored Synthesis of Superparamagnetic Gold Nanoshells with Tunable Optical Properties. *Adv. Mater.* **2010**, *22*, 1905−1909.

(54) Seo, S. B.; Yang, J.; Lee, T.; Chung, C. H.; Song, Y. J.; Suh, J. S.; Yoon, H. G.; Huh, Y. M.; Haam, S. Enhancement of Magnetic Resonance Contrast Effect Using Ionic Magnetic Clusters. *J. Colloid Interface Sci.* **2008**, *319*, 429−434.

(55) Sau, T. K.; Murphy, C. J. Room Temperature, High-Yield Synthesis of Multiple Shapes of Gold Nanoparticles in Aqueous Solution. *J. Phys. Chem. B* **2004**, *126*, 8648−8649.

(56) Lohse, S. E.; Murphy, C. J. The Quest for Shape Control: A History of Gold Nanorod Synthesis. *Chem. Mater.* **2013**, *25*, 1250−1261.

(57) Hao, E.; Schatz, G.; Hupp, J. Synthesis and Optical Properties of Anisotropic Metal Nanoparticles. *J. Fluoresc.* **2004**, *14*, 331−341.

(58) Chen, H.; Shao, L.; Ming, T.; Sun, Z.; Zhao, C.; Yang, B.; Wang, J. Understanding the Photothermal Conversion Efficiency of Gold Nanocrystals. *Small* **2010**, *6*, 2272−2280.

(59) Cole, J. R.; Mirin, N. A.; Knight, M. W.; Goodrich, G. P.; Halas, N. J. Photothermal Efficiencies of Nanoshells and Nanorods for Clinical Therapeutic Applications. *J. Phys. Chem. C* **2009**, *113*, 12090−12094.

(60) Moan, J.; Peng, Q.; Evensen, N. J.; Berg, K.; Western, A.; Rimington, C. Photosensitizing Efficiencies, Tumor and Cellular Uptake of Different Photosensitizing Drugs Relevant for Photodynamic Therapy of Cancer. *Photochem. Photobiol.* **1987**, *46*, 713−721.

(61) Firey, P. A.; Rodgers, M. A. J. Photo-Properties of a Silicon Naphthalocyanine: A Potential Photosensitizer for Photodynamic Therapy. *Photochem. Photobiol.* **1987**, *45*, 535−538.

(62) Cheng, Y.; Samia, A. C.; Meyers, A. C.; Panagopoulos, I.; Fei, B.; Burda, C. Highly Efficient Drug Delivery with Gold Nanoparticle Vectors for *in Vivo* Photodynamic Therapy of Cancer. *J. Am. Chem. Soc.* **2008**, *130*, 10643−10647.

(63) Hauck, T. S.; Jennings, T. L.; Yatsenko, T.; Kumaradas, J. C.; Chan, W. C. W. Enhancing the Toxicity of Cancer Chemotherapeutics with Gold Nanorod Hyperthermia. *Adv. Mater.* **2008**, *20*, 3832−3838.